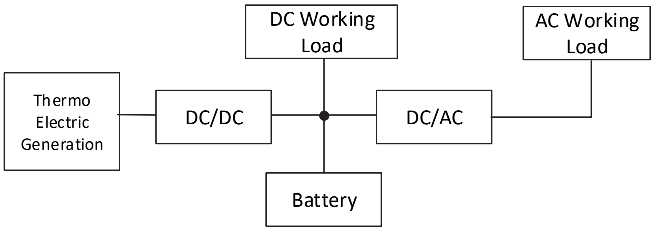


Fig. 1. Block diagram of TGS

are built to verify the effectiveness of the proposed method for improving frequency regulation.

## 2. OVERALL STRUCTURE OF TGS

TGS is mainly composed of thermoelectric panel, system controller, battery, DC voltage regulator, inverter and other parts. The basic composition is illustrated in Fig. 1.

### *2.1 Overview of TGS integrated to SSPS of power plant*

The *SSPS* of a power plant normally has two voltage levels. One is 6kV which is obtained by the generator outlet through 20KV/6KV transformer. The other one is 380V delivered by 6KV voltage bus through 6kV / 380V transformer. As shown in Fig. 2, two options are proposed in the whole system design. Plan I: Combine all thermoelectric generation chips into a group and supply power to 380V working load on one side. Plan II: Divide the thermoelectric generation chips into two groups to supply 380V working load on both sides respectively. The structure is simpler and the investment is lower for Plan I. Plan II is a double supply system that has higher reliability. But the investment is higher. Hence, Plan I is adopted in this work.

### *2.2 Physical layout of TGS*

TGS converts the flue gas of the coal-fired boiler in the power plant to electric power. All the thermoelectric generation components are mainly arranged at the inner wall of the chimney as shown in Fig. 3.

As the temperature of the exhaust gas is high enough, the main concern for the hot end of thermoelectric chip is how to improve the uniformity of the surface temperature. The cold end is usually installed with a heat sink which is cooled by air or water. The forced cooling air is used to improve the temperature difference between the two ends of thermoelectric generation device. At the same time, the cooling air which is heated can be directly transferred to the combustion boiler. It can also improve the combustion condition and make the pulverized coal fully burn.

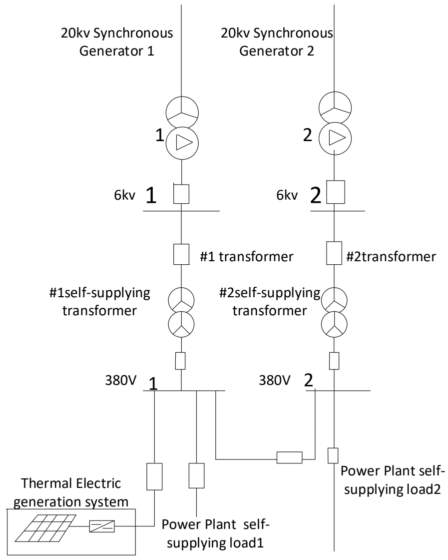


Fig. 2. Diagram of TGS integrated to self-supply power system of power plant

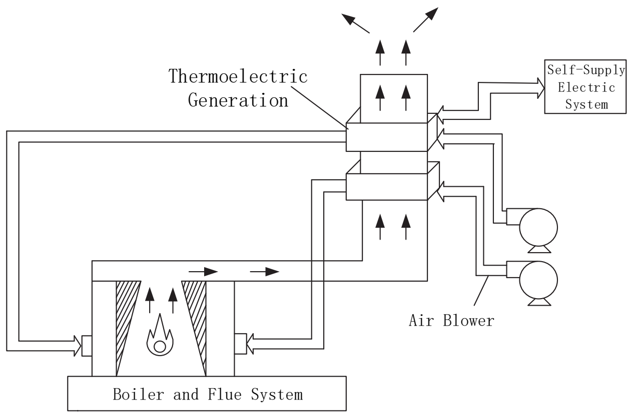


Fig. 3. Physical layout of TGS

## 3. ENHANCED POWER CONTROL BASED ON VSG

### *3.1 Traditional VSG model*

There are two operation modes for the self-supply power system which are grid on and off. The frequency can be supported by the power grid under the grid-on mode. And there is no need to adjust the frequency of the self-supply power system by TGS. For the grid-off mode, the frequency of the self-supply power system is very sensitive to the fluctuation of working load. The frequency fluctuation will affect the safe and stable operation of the whole system. Therefore, how to maintain the frequency stability is one of the key control strategies for the self-supply power system.

Because synchronous generator has the moment of inertia and damping coefficient, it is friendly for the power grid. The method of excitation and frequency control of VSG can be applied to TGS. It can simulate the

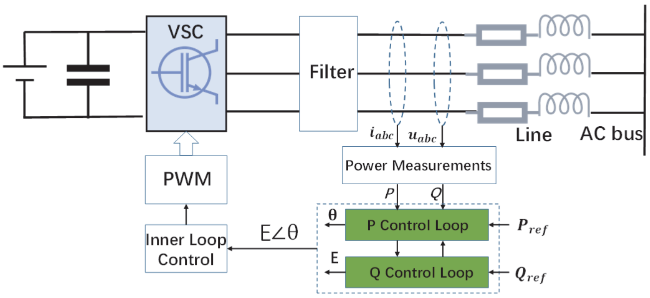


Fig. 4. Overall structure of the VSG system

characters of synchronous generator. The schematic diagram of traditional VSG is shown as Fig. 4.

In Fig. 4, a grid-forming VSC converts the renewable energy into the form of energy that complies with the power grid. A filter built with inductors and capacitors and the line impedance are located between the VSC and the point of common-coupling (PCC). The active-power P control and reactive-power Q control loops (Fig. 5) provide regulations of the frequency (or phase) and voltage magnitude. Various grid-forming control strategies can be implemented in these controllers. The grid frequency and output power are measured by the frequency detector and the power meter blocks, respectively.

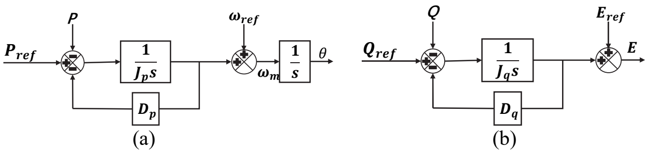


Fig. 5. (a) P control loop and (b) Q control loop

The control algorithm of VSG is shown as equation (1) [12].

$$\begin{cases} J\omega_m \cdot \frac{d\omega_m}{dt} = P_{in} - P + D(\omega_g - \omega_m) \\ \Delta\omega = \omega_m - \omega_g \\ \frac{d\delta}{dt} = \Delta\omega \end{cases} \quad (1)$$

where $J$ is the moment of inertia. $D$ is the damping coefficient. $\omega_g$ is the grid angular frequency. $\omega_m$ is the VSG angular frequency. $P_{in}$ and $P$ are mechanical power and electromagnetic power, respectively. $\delta$ is the power angle.

During transient operations, if the ratio of R to X is unneglectable in the transmission line, the output active-power P and reactive-power Q of the VSG [5] can be expressed as:

$$P = \frac{3EV}{\sqrt{R^2+X^2}}\sin(\delta + \tan^{-1}\frac{R}{X}) - \frac{3RV^2}{R^2+X^2} \quad (2)$$

$$Q = \frac{3EV}{\sqrt{R^2+X^2}}\cos(\delta + \tan^{-1}\frac{R}{X}) - \frac{3XV^2}{R^2+X^2} \quad (3)$$

where $E$ and $V$ are the VSG output voltage and AC bus voltage, respectively. $\delta$ is the phase displacement between $E$ and $V$. It is observed that both P and Q exhibit nonlinear behaviors with sine and cos functions. They are coupled by the mutual influence of the $\delta$ and $E$.

The line reactance is dominant compared to the resistance. Therefore, the equivalent impedance is mainly inductive, which is often justified by the high inductive components in filter-inductor and high-voltage or medium voltage transmission line. In this sense, equations (2) and (3) are simplified into:

$$P = \frac{3EV}{X}\sin(\delta) \quad (4)$$

$$Q = \frac{3EV}{X}\cos(\delta) - \frac{3V^2}{X} \quad (5)$$

Equations (4) and (5) represents a power circle illustrated in Fig. 6 in the *P-Q* reference frame. The circle is centered at $\left[0, -\frac{3V^2}{X}\right]$. The radius is $\frac{3EV}{X}$. In general, the VSG operates in the first quadrant. $P_{max}$ is the maximum active power point where $\delta$ reaches the upper limit with the regulation of $E$. $Q_{max}$ is the maximum reactive power at the voltage levels of $E$ and $V$. It can be demonstrated that the existence of the line resistance reduces $P_{max}$.

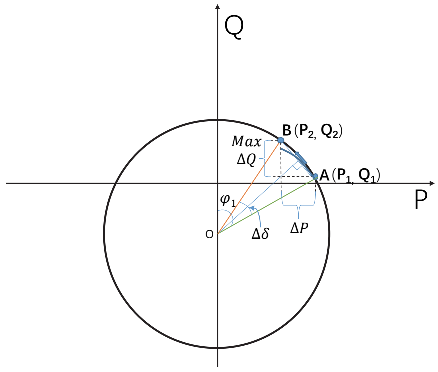


Fig. 6 . The coupling of $\Delta P$ and $\Delta Q$ during a step-down operation of P

### 3.2 *Power Coupling*

To exploit the power coupling on the basis of the graphical model in Fig. 6, it is assumed that the initial working point is at A with the coordinate $(P_1, Q_1)$. Then, in response to the reference step-down of *P*, the *P* control-loop will reduce the power angle to generate less active power. The angle change is denoted as $\Delta\delta$. This perturbation also drives *Q* to change. The *Q* control-loop will see the variation $\Delta Q$ and calculate a new $Q_{ref}$. By using a linear controller such as droop control or PI control etc., the capability of dynamic regulating is limited. *Q* will not be brought back to its normal value rapidly.

This Section is intended to break the linkage of Q and $\Delta\delta$ such that $\Delta Q$ is minimized. The idea is illustrated in Fig. 7. Instead of travelling on the outer circle, the initial operating point A $(P_1, Q_1)$ is forced to move inside the circle towards $B'$ $(P_2, Q_1)$ on the inner circle. Eventually, $\Delta Q$ can be reduced during the transient power change. This indicates that a voltage compensation must be made to remedy the effect of $\Delta\delta$. As $\Delta\delta$ reduces, the radius of the power circle has to be adjusted accordingly to weaken the link of the reactive power and the power angle. An analysis is carried out to verify the reactive power dynamic process after the voltage compensation is added.

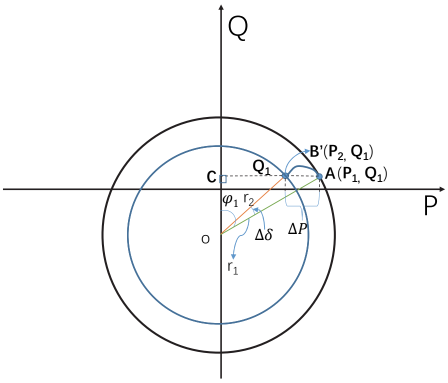

Fig. 7. Decoupling of $\Delta Q$ and $\Delta\delta$

### 3.3 *Power Decoupling*

In the triangle O$B'$A as shown in Fig. 7,

$$\Delta P / \sin \Delta\delta = r_2 / \sin\left(\frac{\pi}{2} - \varphi_1\right) = r_2 / \cos\varphi_1 \qquad (6)$$

where $r_2$ is the radius of the inner circle. $\varphi_1 = \delta_1$.
Hence,

$$\Delta P = r_2 \sin\Delta\delta \,/\, \cos\varphi_1 \qquad (7)$$

Define $A_\delta = r_2 / \cos\varphi_1$. Then $\Delta P = A_\delta \sin\Delta\delta$. The relationship between the outer circle radius $r_1$ and $r_2$ is represented by:

$$r_1 / \sin\left(\frac{\pi}{2} + \varphi_1 - \Delta\delta\right) = r_2 / \sin\left(\frac{\pi}{2} - \varphi_1\right) \qquad (8)$$

This leads to

$$r_2 = r_1 \cos\varphi_1 / \cos(\varphi_1 - \Delta\delta) \qquad (9)$$

Since the radius $r$ is proportional to the VSG output voltage $E$, in response to the change of $\Delta\delta$, a voltage compensation $E_2$ corresponding to $r_2$ is obtained as below,

$$E_2 = E_1 \cos\varphi_1 / \cos(\varphi_1 - \Delta\delta) \qquad (10)$$

$A_\delta$ is also a function of $r_1$ and $\Delta\delta$ that can be expressed as

$$A_\delta = r_1 / cos(\varphi_1 - \Delta\delta) \qquad (11)$$

### 3.4 *Stable P Control-Loop*

The active power $P$ delivered to the PCC is expressed as:

$$P = \Delta P + P_1 = A_\delta \sin\Delta\delta + P_1 \qquad (12)$$

If $\Delta\delta$ varies below $\pi/6$, then (12) becomes:

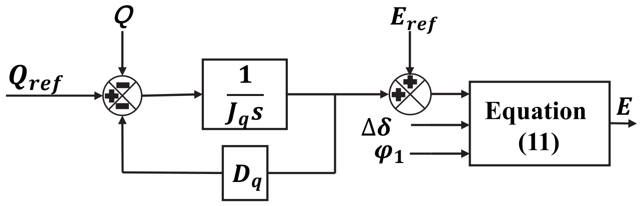

Fig. 8. Voltage compensation Scheme

$$P = A_\delta \Delta\delta + P_1 \qquad (13)$$

The swing equation is written below.

$$J\omega_m \cdot \frac{d\omega_m}{dt} = P_{in} - P + D(\omega_g - \omega_m) \qquad (14)$$

Given that $\Delta\delta = \int(\omega_m - \omega_g)\,dt$, $\omega_g = 2\pi f_0$ and (13), the derivative of (12) is

$$dP/dt = A_\delta(\omega_m - \omega_g) \qquad (15)$$

The 2nd order derivative is derived

$$d^2P/dt^2 = A_\delta d\omega_m/dt \qquad (16)$$

Plug (15) and (16) into (14), a second order differential equation is obtained in terms of P:

$$\frac{J\omega_m}{A_\delta} \cdot \frac{d^2P}{dt^2} + \frac{D}{A_\delta} \cdot \frac{dP}{dt} + P = P_{in} \qquad (17)$$

where $J\omega_m$ is a coefficient that varies together with $\omega_m$. Apply Laplace transformation to (17), the transfer function between $P$ and $P_{in}$ is derived:

$$\frac{P(s)}{P_{in}(s)} = \frac{A_\delta / J\omega_m}{s^2 + (D/J_\omega)s + A_\delta / J\omega_m} \qquad (18)$$

Compared to the standard form of the second order equation, the natural frequency $\omega_n$ and damping factor $\zeta$ are found as below:

$$\omega_n = \sqrt{A_\delta / J\omega_m} \qquad (19)$$

$$\zeta = D/2\sqrt{A_\delta / J\omega_m} \qquad (20)$$

## 4. SIMULATION AND EXPERIMENTAL RESULTS

### 4.1 *Simulation Conditions*

In order to test the effectiveness of the improved VSG control strategy, a simulation model based on MATLAB is built [13]. The simulation parameters are shown as Table 1. The simulation time is set as about 0.8s. VSG operates with a working load of 8 kW at the initial time. The working load is removed by 5kW at 0.3s. Then the working load is restored to be 8kW after 0.6s. The frequency stability caused by working load disturbance is simulated.

Table 1. Parameters of the Simulation Model

| Parameter | Value | Parameter | Value |
|---|---|---|---|
| Rated frequency | 50Hz | DC voltage | 800V |
| Switching frequency | 10KHz | Line inductance | 4*10^-3H |
| Rated AC voltage | 220V | Line capacitance | 30*10^-6F |
| $J_0$ | 0.4 kg·m2 | $D_0$ | 10 N·m·s/rad |

## 4.2 *Simulation results*

As shown in Fig. 9 and Fig. 10, they are the active power and angular frequency waveforms based on the improved VSG and traditional VSG against the same working load disturbance. The angular frequency deviation in Fig. 10 is less than Fig. 9. The adjustment period of Fig. 10 is also less than Fig. 9. Therefore, the dynamic frequency response of the improved VSG is better than the response of traditional VSG. As shown in Fig. 11 and Fig. 12, J and D of the improved VSG can be adjusted automatically according to the working load.

## *4.3 Experimental Results*

An experimental platform is built to validate the improved VSG as shown in Fig. 13. VSG operates with a working load of 300W at the initial time. The load is removed by 150W during working period in islanding

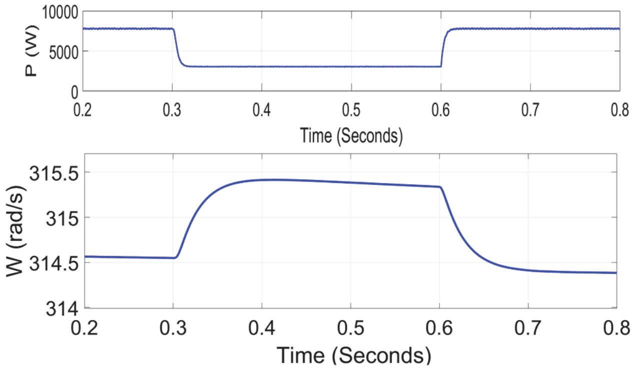


Fig. 9. Active power and angular frequency response without compensation

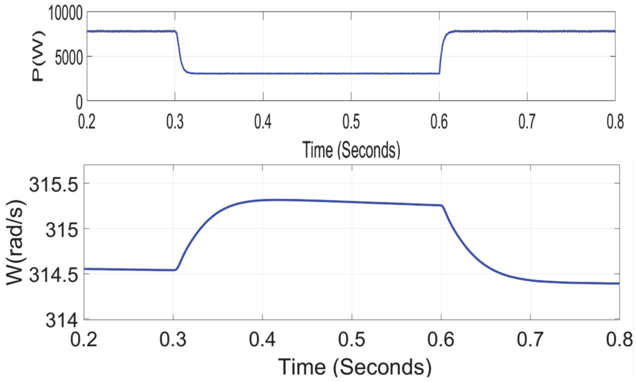


Fig. 10. Active power and angular frequency response with compensation

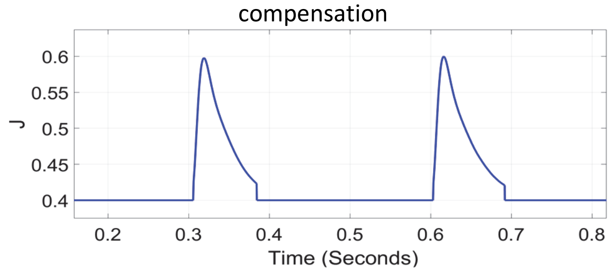


Fig. 11. J under different working load

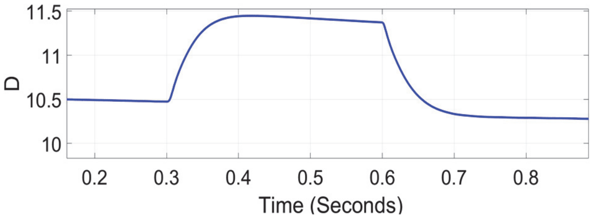


Fig. 12. D under different working load

mode. The angular frequency responses of experimental results are shown as Fig. 14. The angular frequency deviation based on the improved control is less than the traditional control. The angular frequency adjusting time of the improved control is quicker than the traditional control. Therefore, the performance of the angular frequency modulation based on the improved VSG is better than the traditional VSG.

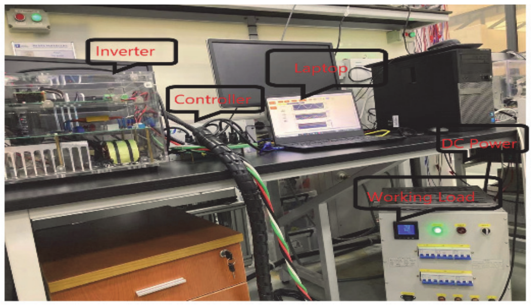


Fig. 13. Experiment Platform.

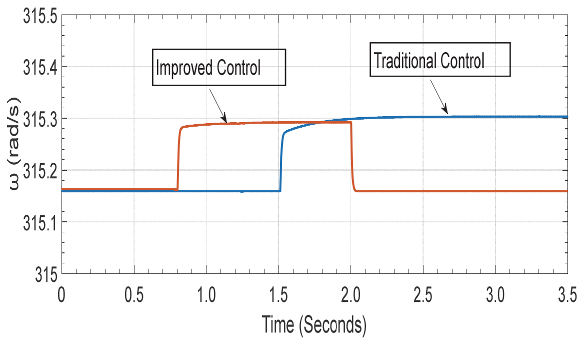


Fig. 14. Angular frequency of experimental results

## *CONCLUSIONS*

The flue gas of the power plant is converted into electrical power by TGS. TGS is integrated to the self-supply power system of the power plant. An improved VSG has been presented in details in the paper. A simulation model and experiment platform have been established for the improved VSG and the traditional VSG under the grid-off mode. The simulation and experiment result show that the improved VSG is able to not only response more qiuckly, but also reduce the static deviation of the frequency. Compared with the traditional VSG, the improved VSG produces better dynamic and static regulation performance for the frequency.

**ACKNOWLEDGEMENT**

This work was supported by Ningbo Science and Technology Bureau under the project No. 202003N4182.

**REFERENCE**

[1] Yan Xiangwu, Zhang Weichao. Review of VSG control-enabled universal compatibility architecture for future power systems with high-penetration renewable generation. Applied Sciences; 2019, 9(7): 1484.

[2] Lopes J A P, Hatziargyriou N, Mutale J, et al. Integrating distributed generation into electric power systems: a review of drivers, challenges and opportunities. Electric Power Systems Research; 2007, 77(9): 1189-1203.

[3] Zhang Weichao, Liang Haifeng, Bin Zhou, et al. Review of DC technology in future smart distribution grid IEEE PES Innovative Smart Grid Technologies, Tianjin, China, 2012: 1-4.

[4] Guarnieri M. More light on information [historical][J]. IEEE Industrial Electronics Magazine; 2015, 9(4): 58-61.

[5] Zhong Qingchang. Power-electronics-enabled autonomous power systems: architecture and technical routes. IEEE Transactions on Industrial Electronics; 2017, 64(7): 5907-5918.

[6] LIU Zong，LI Teng，MU Yong. Research on simulated inertia coordination control strategy of VSG based on energy storage. DES tech transactions on computer science and engineering; 2018（16）：214-220.

[7] MA Yanfeng，LIN Zijian，YU Rennan，et al. Research on improved VSG control algorithm based on capacity-limited energy storage system. Energies; 2018，11（3）：16-21.

[8] Y. Hirase, O. Noro, K. Sugimoto, K. Sakimoto, Y. Shindo and T. Ise. Effects of suppressing frequency fluctuations by parallel operation of virtual synchronous generator in microgrids; 2015 IEEE Energy Conversion Congress and Exposition (ECCE), Montreal, QC; 2015, pp. 3694-3701.

[9] J. Alipoor, Y. Miura and T. Ise. Distributed generation grid integration using virtual synchronous generator with adoptive virtual inertia; 2013 IEEE Energy Conversion Congress and Exposition, Denver, CO, 2013, pp. 4546-4552.doi: 10.1109/ECCE.2013.6647309

[10] CHENG C，YANG H，ZENG Z，et al. Rotor inertia adaptive control method of VSG. Automation of electric power systems; 2015，39（19）：82-89.

[11] SONG J，ZHANG H，SUN K，et al. Improved adaptive control of inertia for virtual synchronous generators in islanding micro-grid with multiple distributed generation units. Proceedings of the CSEE; 2017，37（2）：412-423.

[12] Zhong Q C，Weiss G．Synchronverters：Inverters that mimic synchronous generator. IEEE Transactions on Industrial Electronics; 2011，58(4)：1259-1267．

[13] Du Y，Guerrero J M, Chang L C，et al．Modeling，analysis，and design of a frequency-droop-based virtual synchronous generator for microgrid applications. Proceedings of ECCE Asia．Melbourne，VIC：IEEE; 2013：643-649．

[14] Sun Y X, Chen C, Shi K, et al. Rotational Inertia Adaptive Control Strategy for Virtual Synchronous Generator Based on Island Operation. Proceeding of the CSU-EPSA: 2019, 1-6.